Measurement 234 (2024) 114792

Contents lists available at ScienceDirect

Measurement

journal homepage: www.elsevier.com/locate/measurement

# Characterizing in-band full-duplex in broadcast communications: From field trials to a loopback channel model

Iñigo Bilbao [a], Eneko Iradier [a,*], Marta Fernandez [a], Jon Montalban [a], Pablo Angueira [a], Zhihong Hunter Hong [b], Yiyan Wu [b]

[a] University of the Basque Country (UPV/EHU), Spain
[b] Communications Research Center Canada, Ontario, Canada

ARTICLE INFO

*Keywords:*
Channel modeling
Characterization
Delay spread
Field trials
Full-duplex
IBFD
IDL
ITCN
k-factor
Loopback
Self-interference
Signal isolation

ABSTRACT

In-band full duplex (IBFD) communications are a potential solution to spectrum scarcity. IBFD communications offer greater spectral efficiency than traditional half-duplex communications by transmitting and receiving on the same frequency channel. However, IBFD operation requires overcoming the challenge of eliminating the self-interference coupled from the transmit antenna to the receive subsystem. Knowledge of the characteristics of the loopback propagation channel makes it easier to cancel out the self-interference. Nevertheless, complex field trials are required to adequately characterize loopback channels, which is still lacking in the recent literature. This paper proposes a measurement campaign in a real and ongoing broadcast transmission center to characterize the main characteristics of loopback channels. The work proposes a set of loopback channels based on field trials and an empirical analysis of the most relevant parameters of the channel model, such as the Doppler spectrum, the delay spread, and the K-factor.

## 1. Introduction

The increased demand for new applications and the augmented consumption of high-data-rate multimedia services drive the permanent evolution of wireless communication systems. Without a doubt, many of the recent advances are remarkable, such as coding [1,2] or multiplexing schemes [3,4]. The success of many of these advances is closely related to the reliability of laboratory tests and field trials. Both to test their performance in real-world environments and to learn as much as possible from the environment in which they are deployed.

Concerning the physical layer (PHY), although traditional signal processing has continuously improved the performance, it is already very close to the Shannon limit, so the improvement margin is minimal [5]. In addition, due to spectrum scarcity, the limitations of using the radio spectrum must also be considered when targeting system efficiency [6]. Techniques such as in-band full-duplex (IBFD) communications can be decisive in meeting future spectrum needs [7–9].

An IBFD system simultaneously transmits and receives signals within the same radio frequency (RF) channel. Thus, theoretically, IBFD could double the spectral efficiency if compared with half-duplex systems [10]. The increased spectral efficiency opens the door to new use cases and bands limited by the capacity of current half-duplex systems. Several authors have already proposed and evaluated IBFD in combination with different wireless communication standards. In particular, several measurement campaigns have shown the applicability and challenges of IBFD in diverse applications, such as Wi-Fi [11–14], satellite communications [15,16], wearable applications [17], and 5G/6G [18–21].

One of the standard families that have evolved significantly over the last decade is terrestrial broadcasting [22]. Traditional DTT standards are one-way (i.e., downlink-only mode), limiting the number of possible services. This limitation has been addressed by pushing for incorporating new IBFD-based solutions. Recent examples include the in-band distribution link (IDL) system and the inter-tower communications network (ITCN) proposal. IDL is a one-way wireless content distribution system that replaces the studio-to-transmitter link (STL) via microwave or fiber [23,24]. ITCN aims to interconnect all broadcast towers to create a communication network for control, monitoring, data communication, localized datacast, and broadcast services [25]. IBFD communications will be used to manage the simultaneous transmission of the ongoing broadcast content, ITCN, and IDL data and will open the door to future architectures [26]. Fig. 1 shows a representation of an ITCN implementation using two transmission towers. As the

* Corresponding author.
*E-mail address:* eneko.iradier@ehu.eus (E. Iradier).

https://doi.org/10.1016/j.measurement.2024.114792
Received 20 February 2024; Received in revised form 8 April 2024; Accepted 25 April 2024
Available online 27 April 2024
0263-2241/© 2024 The Authors. Published by Elsevier Ltd. This is an open access article under the CC BY-NC-ND license (http://creativecommons.org/licenses/by-nc-nd/4.0/).


**Fig. 1.** Representation of an ITCN application combining DTT content transmission and ITCN communications between TX1 and TX2.

figure shows, two services are combined: ITCN content transmission that interconnects the transmitters (i.e., TX1 and TX2) and each tower's DTT content delivery to the surrounding users.

Although IBFD-based applications have a promising future, cancellation of the loopback signal or self-interference (SI) must be addressed in realistic environments. The loopback self-interference is caused by the signals leaking from the node's transmission into its reception chain. As shown in Fig. 1, each transmitter is simultaneously transmitting (i.e., DTT content) and receiving (i.e., ITCN content). Some locally transmitted DTT power is leaked into the ITCN antenna receiver, generating interference. Generally, IBFD communications need cancellation modules to decrease the impact of the loopback signal [27–29]. Several cancellation techniques are considered blind or semi-blind, not requiring estimating the channel impulse response, [30–32]. Nevertheless, most of them increase their performance when the loopback channel is known [33,34].

As authors in [35] described, SI cancellation techniques can be classified into three main groups: propagation, analog, and digital domain cancellation. First, propagation domain techniques are related to the infrastructure and the elements involved in the communications and can be divided into passive and active techniques. On the one hand, the passive techniques focus on optimizing the antenna systems and minimizing self-interference coupling [36]. On the other hand, some of the most common active techniques are impedance tuning, antenna coupling networks, or cross-polarization controlling devices. Although field trials have been conducted in various environments [37–40], all studies highlight the difficulty of measurement due to complex access and lack of characterization. In addition, the work in the literature has only characterized the power isolation between transmitting and receiving antennas.

Then, analog cancellation techniques refer to the signal processing carried out in the analog domain, mainly on the RF sections of the receiver chain. They can be developed in frequency and time domains and offer a helpful alternative to digital domain cancellation modules with large dynamic range requirements [41]. Typically, analog cancellation techniques improve the transmitted–received ratio for a frequency band of around 15–40 dB. They are usually implemented with passive cancellation techniques to increase the performance rate to 80 dB [42–44]. Nevertheless, the success of the analog interference cancellation algorithms lies in the precise knowledge of the channel impulse response [45–47]. Therefore, proper channel estimation and representative reference channel models are critical.

Digital domain techniques refer to channel modeling and digital cancellation. Generally, digital cancellation techniques outperform analog methods [48]. Software-based processes have fewer operation limits than hardware-based ones, and several studies have demonstrated that it is possible to overcome the 50 dB performance barrier using only digital cancellation [23,49]. Nevertheless, as in the case of analog cancellation, the accuracy of the loopback channel estimation is vital for high-performing interference cancellation systems [50–52].

Considering all the above, there is a need to characterize the loopback channel of IBFD transmitters. Although some IBFD-related research works have used loopback channel models [27,30], there is not an accurate characterization of the most relevant aspects of a wireless propagation channel, such as the delay spread, K-factor, and Doppler spectrum. Only transmitter and receiver system isolation has been studied in previous works [40]. The present study proposes a complete characterization of a loopback channel model based on empirical data obtained from a measurement campaign and combining various proposals in previous works [53–56]. To the authors' knowledge, this paper presents the first characterization of a loopback channel model based on experimental measurements in an actual and ongoing transmission infrastructure. The work presents the methodology followed during the field trials, the results obtained when characterizing the channel, and an analysis of different parameters that characterize the channel, such as the Doppler spectrum, the delay spread, or the K-factor. In summary, the technical contributions of this paper include the following:

- A new methodology for measuring and characterizing broadcast loopback channels.
- Characterizing the loopback channel in terms of the amplitude and the delay of the paths.
- An analysis of the obtained delay spread and K-factor values.
- Characterizing the Doppler spectrum of the loopback channel in broadcast transmitters.
- Performance evaluation of the proposed channel models under an ATSC 3.0 compliant transceiver chain.

The rest of the paper is organized as follows. The next section describes the system model of the IBFD systems and the multipath channels. Then, Section 3 presents the measurement methodology followed during the field trials. In Section 4, the obtained channel model is characterized, analyzed, and discussed. Section 5 presents the performance evaluation of the proposed channel models. Finally, the conclusions of this paper are summarized in Section 5.

## 2. System model

This section presents the IBFD system model proposed in this work. First, the general concepts of the system model are described, and later, the tapped delay line (TDL) propagation channels are presented from the perspective of in-band full-duplex communications.

### 2.1. General concepts

In-band full-duplex communications simultaneously handle data flows in both uplink and downlink directions. Therefore, the nodes participating in full-duplex communications are receivers and transmitters simultaneously and within the same bandwidth. Part of the transmitted signal will be leaked from the transmitting radiation system to the receiving antenna, generating self-interference. From here on, we will refer to the self-interference signal as the loopback signal (LBS). Thus, the received signal comprises two parts, one related to the desired

or forward signal (FWS) and the other to the loopback signal. This situation in the frequency domain can be described as follows:

$$Y(k) = X_{FWS}(k) \cdot H_{FWS}(k) + \eta \cdot X_{LBS}(k) \cdot H_{LBS}(k) + N_0(k), \quad (1)$$

where $X_{FWS}(k)$ and $X_{LBS}(k)$ are the desired forward signal and the loopback signal, respectively. $H_{FWS}(k)$ and $H_{LBS}(k)$ are the desired forward signal channel response and the loopback channel response in the $k$th subchannel, respectively, $\eta$ is the power ratio between the forward and loopback signals, and $N_0$ is the Additive White Gaussian Noise (AWGN) noise.

The $X_{FWS}$ information is decoded only after eliminating the loopback component. Several signal cancellation techniques exist for loopback elimination in analog and digital domains. However, these methods necessitate an accurate estimation of the loopback channel to achieve optimal performance [27–29,33,34]. In general, a model of the loopback signal is generated, and the channel effects (such as attenuation, delay, and phase shift) are applied. Each temporal component (tap) of the created signal to cancel can be described as follows:

$$s(t) = \alpha \cdot x_{LBS}(t - \psi)e^{j\phi}, \quad (2)$$

where $\alpha$ is the amplitude, $\psi$ is the time delay and $\phi$ is a phase shifter.

Subsequently, the cancellation signal is combined with the received signal in the time domain:

$$y'(t) = y(t) - s(t), \quad (3)$$

where $y'$ is the remaining signal after cancellation. In an ideal scenario, the objective of the cancellation signal is to eliminate the impact of the loopback signal (expressed as $\eta \cdot x_{LBS}(t) * h_{LBS}(t)$). However, seeking an exact replica of the coupled signal is impractical. Consequently, the signal that remains after the cancellation process can be characterized as follows:

$$y'(t) = x_{FWS}(t) * h_{FWS}(t) + n_C(t) + n_0(t), \quad (4)$$

where $n_C$ is the non-ideal cancellation residue. It is important to note that $n_C$ represents an interfering term and does not have the same effect as $n_0$. This means that $n_C$ does not strictly follow a Gaussian distribution. Specifically, $n_C$ contains a portion of the loopback signal that has not been fully canceled, although it is attenuated compared to the previous step (see Eq. (1)). However, depending on the effectiveness of the cancellation technique, it may fall below the noise floor.

In summary, to achieve optimal loopback cancellation performance, minimizing the cancellation term ($n_C$) is necessary, which is closely tied to the effectiveness of the associated signal processing. The overall performance varies based on the specific algorithm [41], but a consistent rule applies the more accurate the channel estimation, the better the performance. Therefore, obtaining a realistic characterization of the loopback channels remains crucial.

### 2.2. TDL channels

Time-varying and multipath propagation channels are generally described using TDL models. A TDL model consists of discrete paths with specific amplitude and delay. In addition, each path has an associated Doppler spectrum modeling the time-variability of the path amplitude. The generic TDL model can be described as [57]:

$$h(t, \tau) = \sum_{k=0}^{N-1} a_k(t)\delta(\tau - \tau_k), \quad (5)$$

where $N$ is the number of paths, $a_k$ represents the time-varying signal $k$th reflected path, and $\tau_k$ is the relative delay of the reflected path. In this case, $k = 0$ represents the direct signal from the transmitter, so there is no relative delay (i.e., $\tau_0 = 0$).

$H_{FWS}$ and $H_{LBS}$ can be modeled following the mathematical structure of TDL models (as in Eq. (5)). However, the direct and the loopback channels have several differences due to the nature of the use case. In particular, due to the infrastructure of transmission towers, $H_{FWS}$ will have a more substantial multipath effect than $H_{LBS}$. This effect is typically appreciated in the root mean square (RMS) delay spread ($\tau_{RMS}$) since it measures the channel's average delay spread. Therefore, the difference between the $\tau_{RMS}$ measured for both channels, $H_{FWS}$ and $H_{LBS}$, is as follows:

$$\tau_{RMS,FWS} \gg \tau_{RMS,LBS}. \quad (6)$$

If we analyze $\tau_{RMS}$ in more detail, we can conclude that the delay and the amplitude of the received paths define the final $\tau_{RMS}$ value. Consequently, the difference between $H_{FWS}$ and $H_{LBS}$ can be described as:

$$N_{FWS} \gg N_{LBS}, \quad (7)$$

where $N_{FWS}$ and $N_{LBS}$ are the number of paths in the forward and loopback channels, respectively. Furthermore, the maximum delay of the reflected paths will be higher in the forward channel:

$$\max_{FWS}(\tau_k) \gg \max_{LBS}(\tau_k). \quad (8)$$

Lastly, one of the particular characteristics of the loopback channel in TDLs is the first path received (k=0). Since although in both $H_{FWS}$ and $H_{LBS}$, the first path is the beam with the highest energy, they do not have the same characteristics. Generally, in the direct channel, the first path is the line-of-sight component, while in $H_{LBS}$, it is not line-of-sight since the transmission and reception radiating systems are in the same tower but disoriented.

## 3. Measurement system

This section presents the methodology proposed for empirical data recording. In particular, the field trials' basic design and hardware equipment are presented. This measurement campaign was carried out on a transmitter site of a network operator (Itelazpi) [58]. This company provides radio, television, and public communications services.

Fig. 2 shows a conceptual diagram of the measurement methodology followed during this work, while Fig. 3 presents the actual implementation at the transmission center. The first element in Fig. 2 is signal generation. The reference source is a DVB-T2 signal. Some configurable parameters of the DVB-T2 emission are critical to getting the best channel characterization. QPSK 1/2 was used as the modulation and coding rate to generate a robust transmission signal. Then, we selected a high FFT size (i.e., 32 K) to have the highest possible number of subcarriers and, therefore, to increase the channel frequency definition. Table 1 presents the rest of the waveform generation parameters. The measurement system creates a pre-recorded file with In-phase and Quadrature (IQ) samples to be fed into the transmitting antenna using a Dektec DTU-215 (output bandwidth 8 MHz, output power −49 to −18 dBm). After passing through the transmitter site loopback channel, the received signal IQ components are recorded using a vector signal analyzer. The modulator and the generation software are identified in Fig. 3 using a red dashed box.

An additional amplification stage and channel filtering are required before feeding the test signal into the site transmission system. The amplifier is a Promax DT-730 [59] with a gain equal to 52 dB, whereas the channel filtering is tuned to channel 27 on the UHF band. The amplifier is highlighted in yellow Fig. 3.

Además, habrías que destacar que

As shown in Fig. 4, the measurements were carried out in a real and ongoing transmission center with two radiating systems. The highest transmission system (i.e., TX 1, in Fig. 4) is installed at the height of 25 m, whereas the second transmission system (i.e., TX 2, in Fig. 4) is 23 m high. Each transmission system can be used in a single frequency. In particular, the center frequency of TX 1 is 522 MHz, while TX 2 uses 514 MHz. The radiating system installed on the tower comprises four sectors (i.e., panels located at 50°, 140°, 230°, and 320°), and each sector uses two panels per bay, improving directivity on the vertical plane.

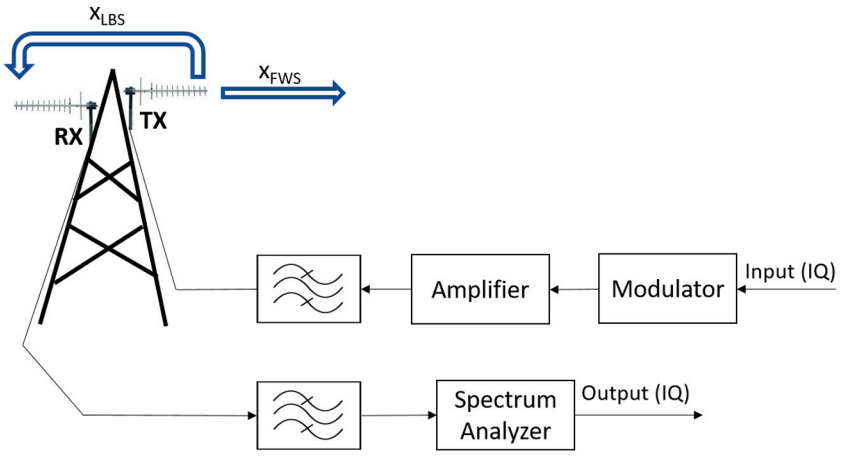


**Fig. 2.** Block diagram of the complete transmission-reception chain implemented for the channel measurement campaign.

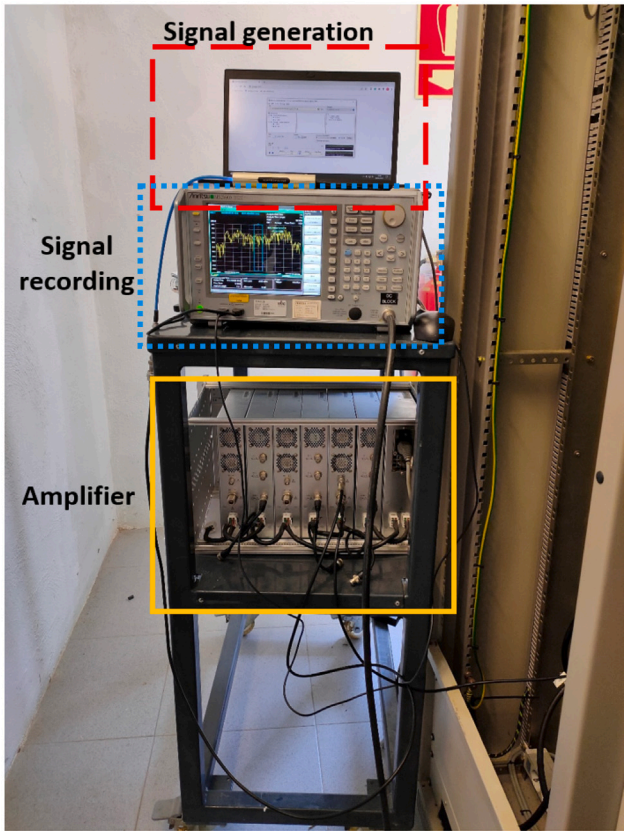


**Fig. 3.** Transmission-reception chain implementation using hardware equipment. The three principal stages for channel measuring are highlighted: signal generation, amplification, and recording.

**Table 1**
Summary of the configuration parameters used for signal generation.

| Parameter | Value |
|---|---|
| FFT size | 32 k |
| Guard interval | 1/16 |
| Bandwidth | 8 MHz |
| Pilot pattern | PP2 |
| Modulation | QPSK |
| Code rate | 1/2 |
| L1 Modulation | BPSK |
| Rotated cons. | No |
| #Superframes | 1 |
| #Frames per superframe | 2 |
| #Data symbols | 63 |
| Superframe length | 488 ms |

Panels are Rymsa 6xAT15-250, which are composed of four dipoles. Each panel has a 3 dB beamwidth of 61° and 27° in the horizontal and vertical planes, respectively, and a gain of 11.1 dB referenced to the $\lambda/2$ dipole. These panels have a dimension (i.e., width × height × depth) of 483 × 264 × 983 mm and a weight of 13 kg. It should be highlighted that as a fully operational broadcast site, each radiating system delivers a set of specific RF channels. In our case, we used TX 1 as the main transmitter; therefore, the working frequency was 522 MHz. One of the main challenges of measuring in real broadcasting facilities is having an adaptable receiver. In this case, we used a single panel for the signal reception (see Rx in Fig. 4). The distance between the transmission system used (i.e., TX 1) and the receiver antenna was 10 m, meaning that the antenna was installed at 15 m. All the radiating systems have horizontal polarization.

The signal passed through a bandpass filter on the reception side to remove potential external co-channel interferences. A vector signal analyzer (Anritsu MS2690 A) sampled the received signal. This stage is identified by a dashed blue line in Fig. 3. The measured IQ data are recorded on a 32-bit float binary format. An automatization process is applied to take periodical recordings of the received signal. Five seconds of the signal are recorded each minute, and overall, the measurement process lasts one hour.

The measurements were taken twice to record data in two scenarios and UHF channels. In the first case, the receiving antenna was oriented to an open area (car parking area). This antenna configuration is displayed in Fig. 4. The second measurement was recorded after rotating the receiver antenna 180° on the horizontal plane (the antenna points to a mountainous area). This way, two different propagation channels for the loopback path should be discussed. From now on, the propagation path where the antenna is facing the car parking will be called Loopback Channel Model 1 (LCM1), and the channel facing the mountain area will be referred to as Loopback Channel Model 2 (LCM2).

The recorded data underwent offline post-processing using specialized software for demodulating and decoding the DVB-T2 signal [60]. This process yielded detailed insights into all decoding stages, including channel estimation based on scattered pilots in both time and frequency domains. The software platform offers various time and frequency interpolation methods, with linear interpolation being the preferred choice recommended by the DVB-T2 implementation guidelines [61]. The selection of the pilot pattern significantly influences the granularity

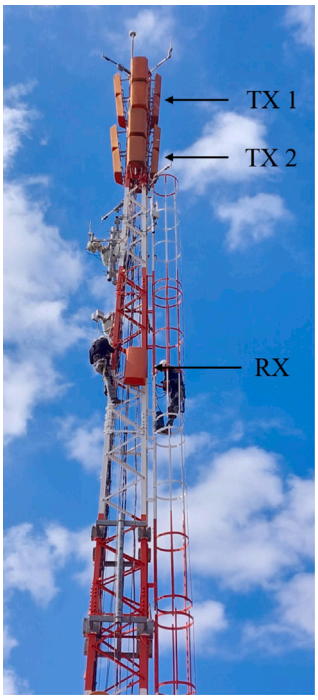


**Fig. 4.** The ongoing broadcast transmission tower during the measurement campaign. The transmission radiating system (TX 1 and TX 2) and the portable receiver (RX) are identified.

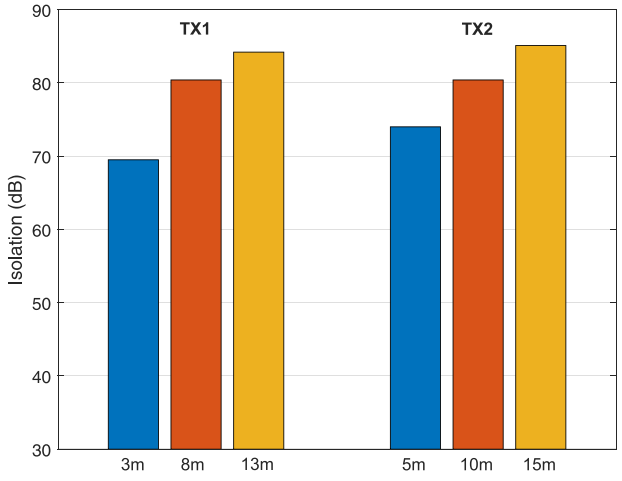


**Fig. 5.** Measured signal isolation using TX 1 and TX 2 and different antenna separation between transmitter and receiver.

of the estimated channel impulse response and associated Doppler mode. In our case, we configured the transmission signal with the PP2 pilot pattern (see Table 1), which involves a low separation of pilot-bearing carriers ($D_x = 6$) and a low sequence length in symbols ($D_y = 2$). This configuration provides the highest channel information (approximately 8.33% scattered pilot overhead) while minimizing the number of required symbols among all possible pilot patterns. For further details about the DVB-T2 receiver platform, refer to the source [60].

Finally, we carried out some signal isolation measurements to test the accuracy of the designed methodology in the transmission tower. The transmission power was set to 30 dBm, and the signal isolation was calculated as the difference between the transmitted signal power and the received power in the channel bandwidth. Fig. 5 shows the results using TX 1 and TX 2 and different TX-RX antenna separations. Minimum signal isolation is close to 70 dB, while the maximum reaches 85 dB. Moreover, increasing the antenna separation increases the isolation, indicating correct behavior. Additional information on the methodology for calculating signal isolation, signal power strength levels, and variability can be found in [40].

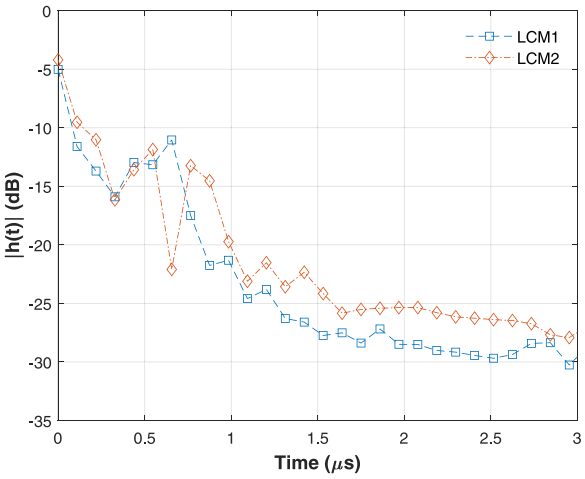


**Fig. 6.** Representation of the average loopback channel model LCM1 and LCM2.

**Algorithm 1** Channel modeling algorithm.

**Define:** $n_p$. The number of paths of the resulting channel model;
**Define:** $N$. The number of samples in the average channel response;
**Define:** $h_f = h_{f,1},...,h_{f,N}$. Set of $N$ samples in the frequency domain response;
**Initialization:** Calculate $h_f$ from the DVB-T2 receiver platform channel estimations;
$h_t = iff t(h_f)$;
**while** $N > n_p$ **do**
    $min_{pos}$ =Position[min($|h_t|$)];
    $h_t(min_{pos} - 1) = h_t(min_{pos} - 1) + h_t(min_{pos})$;
    remove($h_t(min_{pos})$);
    $N = N - 1$;
**end while**

## 4. Channel model characterization and analysis

This section shows the main results obtained from the loopback channel characterization. First, the obtained channel model is described, and then some relevant channel characteristics are derived: Doppler spectrum, delay spread, and K-factor.

### 4.1. Path model

An averaging process has been followed to decrease the impact of additional noise added to the channel input response captured by the DVB-T2 receiver platform. In addition, as will be shown in Section 4.2, the averaging process is feasible because of the low channel variability of the measurements (the Doppler effect is negligible). Fig. 6 shows the results for both LCM1 (blue line) and LCM2 (red line). As expected, the channel impulse responses concentrate most energy in the first path. Later, both channels show reflected paths between 0.3 μs and 1 μs. Then, the channel response falls, and after 1.5 μs, a flat response can be assumed. Moreover, the amplitude difference after 1.5 μs with the maximum ($t = 0$) is between 20–25 dB.

Fig. 6 displays a channel model associated with each case under analysis (i.e., LCM1 and LCM2). The study by Candel et al. [62] has

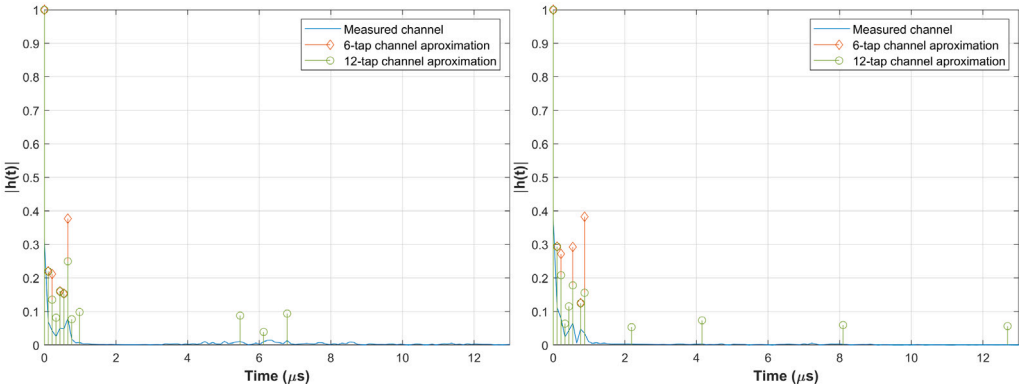


**Fig. 7.** Combined representation of the average channel models LCM1 and LCM2 in linear units and the obtained channel approximations using 6 and 12 taps for each channel model.

**Table 2**
Description of the obtained channel models in terms of tap delay and amplitude.

| | Taps | Tap delay (μs) | Tap amplitude (dB) |
|---|---|---|---|
| LCM1 | 6 | 0, 0.11, 0.22, 0.44, 0.55, 0.66 | 0, −6.6, −6.7, −8.0, −8.1, −4.2 |
| LCM1 | 12 | 0, 0.11, 0.22, 0.33, 0.44, 0.55, 0.66, 0.77, 0.98, 5.47, 6.13, 6.78 | 0, −6.6, −8.7, −10.9, −8.0, −8.1, −6.0, −11.1, −10.0, −10.6, −14.1, −10.3 |
| LCM2 | 6 | 0, 0.11, 0.22, 0.55, 0.77, 0.88 | 0, −5.3, −5.7, −5.3, −9.0, −4.2 |
| LCM2 | 12 | 0, 0.11, 0.22, 0.33, 0.44, 0.55, 0.77, 0.88, 2.19, 4.16, 8.10, 12.69 | 0, −5.3, −6.8, −11.9, −9.4, −7.5, −9.0, −8.1, −12.7, −11.3, −12.2, −12.5 |

been used as a reference to translate the loopback channel function into a channel model with a determined number of paths, amplitude, and phase values. A pseudo-code summary of the algorithm is presented in Algorithm 1.

The algorithm starts defining some relevant parameters, such as the number of paths used to model the loopback channel (i.e., $n_p$), the number of samples that compose the average channel response (i.e., $N$), and the complex values of the frequency domain average channel (i.e., $h_f$). During the initialization stage, we compute the average channel in the frequency domain by taking the mean of all channel estimation values obtained from the DVB-T2 receiver platform. Each channel sample in the frequency domain is averaged to perform this operation. The cost of this operation is determined by the number of samples in the frequency domain ($N$) and the number of channels obtained during the estimation phase ($M$). As a result, the averaging cost is $O(N \cdot M)$. Afterward, the first operation for the channel model is to obtain the time domain response (i.e., $h_t$) by applying the inverse fast Fourier transform (IFFT) to the frequency domain response. Next, a loop is executed while the number of channel samples (i.e., $N$) is higher than the number of paths of the loopback channel model (i.e., $n_p$). In each loop lap, the algorithm finds the position of the $h_t$ sample with the lowest amplitude (see Line 7) and adds the minimum sample value to the adjacent sample (see Line 8). Then, it removes the sample with the lowest amplitude from the average channel response (see Line 9) and decreases the number of samples in the average channel response due to the removal (see Line 10). Finally, when the while loop finishes, $h_t$ contains a set of $n_p$ samples with the most representative time domain response information.

The algorithm's cost primarily depends on $N$, as this parameter determines the number of iterations in Algorithm 1. Consequently, the algorithm's complexity can be expressed as $O(N)$. However, both components must be combined when incorporating the loopback channel averaging as part of the total cost. Thus, the overall algorithmic cost can be expressed as $O(N \cdot M + N)$.

As described in Algorithm 1, the number of taps used to model the channel is a predefined value. The loopback channel has a low multipath effect due to its characteristics, so $n_p$ can be a low value. To be sure to choose a representative value, we have used other existing and widely used channels in the literature as a reference. In particular, several models such as Typical Urban-6 (TU-6), Portable Indoor (PI), and Portable Outdoor (PO) channels [63] have been characterized with 6 or 12 taps and their performance accuracy has been widely demonstrated. Consequently, Fig. 7 shows the channel approximations obtained with Algorithm 1: LCM1 in Fig. 7(a) and LCM2 in Fig. 7(b). Moreover, Fig. 7 also shows two approaches for each channel using 6 and 12 taps.

In addition, based on the obtained channel impulse responses in Fig. 7, most of the channel energy is in the first μs, which implies that fewer approximation taps are required than in high multipath effect channel models. The main reason for using two different approaches is the complexity involved in each of them. Using the model based on six taps in any other communication simulator is less expensive than the 12 taps model, especially from the computational cost point of view. However, the more taps used to model, the more closely it resembles the actual channel. For this reason, we have proposed two different models for the loopback channel that can be adapted to the needs and conditions of each particular case.

The specific values of the channel taps are in Table 2. The table describes each tap's time location (tap delay in μs) and amplitude (tap amplitude in dB). LCM1 and LCM2 present multipath components with significant delay. In particular, the last taps of LCM1 are located between 5-7 μs and around 12 μs for LCM2. However, these taps are less relevant than the energy received with a short delay and become noticeable only when the number of modeling taps rises from 6 to 12. Furthermore, short delay echoes are related to direct loopback leakage. In contrast, long delay echoes are created by multipath reflections of the loopback signal due to the environment. In addition, it should be

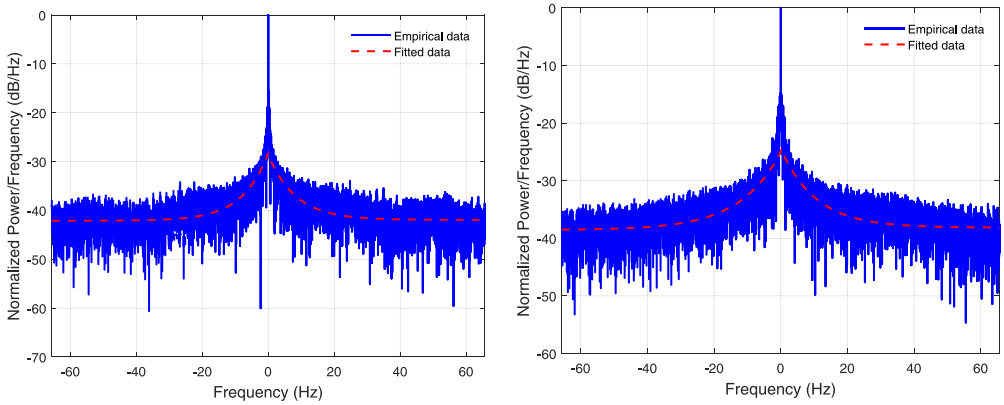


**Fig. 8.** Comparison between the Doppler power spectral density obtained from the empirical data and the exponential fitting curve corresponding to each channel model following Eq. (9).

noted that, in general, both channels present short-distance echoes. In particular, results are aligned if we compare the results with the channel models used in order DTT standardization processes. Other channel models, such as DVBT-P [61] or the TU-6, present most of the received power concentrated within the first few μs. Channel model proposals like the ones developed for DVB-H [63] show the same behavior, where, in addition to the TU-6 channel model, two additional channels were proposed (i.e., Portable Indoor and Outdoor channels, PI and PO), characterized by 12 taps, and concentrate most of the channel energy in the first taps.

### 4.2. Doppler spectrum

A full characterization of the channel model requires a description of the time evolution of the received signal components. Several works have modeled the Doppler power spectral density (PSD) in different applications such as mobile-to-mobile [64], vehicle-to-vehicle [65], and other systems. Several classical models are widely accepted to model PSDs in transmission/reception chain simulations (e.g., Jakes, Laplacian, Gaussian, or flat Doppler spectrums) [66].

Classical models do not always fit the real-time evolution of the propagation channel. In those cases, authors usually model their system with empirical data. For example, authors in [53,54] presented their PSD model with empirical measurements. Based on the characteristics found in the obtained data, the authors defined their PSD with a Dirac delta for $f = 0$ Hz and exponential fittings for both the negative and positive frequencies. In particular, the PSD model was mathematically defined as follows:

$$S(f) = \begin{cases} a\,\exp(bf) - c, & f_{min} \le f < 0 \\ \delta(f), & f = 0 \\ d\,\exp(-ef) - g, & 0 < f \le f_{max} \end{cases} \tag{9}$$

where $a$, $b$, $c$, $d$, $e$ and $g$ are positive constants, $f$ is the Doppler frequency (Hz), and $f_{max}$ and $f_{min}$ are the maximum and minimum frequency values. $b$ and $e$ represent the exponential decay (the lower values, the broader spectral characteristics). $c$ and $g$ are related to the asymptotic values for infinite negative and positive frequencies, respectively. Then, $a$ and $d$ account for the relative value of the curve for the $y$-axis concerning the asymptotic values for infinite frequencies given by $c$ and $g$. This way, the PSDs are obtained in dB/Hz after normalization concerning the main component, which is obtained for $f = 0$ Hz.

The PSD models described by Eq. (9) accurately represent the Doppler spectrum of pseudo-static environments. This is because the static component (i.e., $f = 0$ Hz) contains most of the power, and as we move away from that point, the power drops rapidly. For this work, Eq. (9) was used as a reference PSD model because broadcast environments exhibit these characteristics. The Doppler spectrum exhibits minimal variability in environments with few mobile elements and highly directional communications. As a result, the $f = 0$ Hz component is the most significant of the spectrum.

Since the PP2 pilot pattern has been selected, we have a channel estimation for every two symbols (i.e., $D_y = 2$). So, the channel estimation period can be calculated as follows:

$$T_{est} = D_y \cdot (T_U + T_G) = 2 \cdot (3.584 + 0.224) = 7.616 \text{ ms}, \tag{10}$$

where $T_U$ and $T_G$ are the symbol time and the guard interval, respectively. The exact values are defined in [61]. Therefore, the Doppler frequency range can be calculated as follows:

$$f_D = \pm\frac{1}{2} \cdot \frac{1}{T_{est}} = \pm 65.65 \text{ Hz}, \tag{11}$$

where the ends of the range are the maximum and minimum Doppler frequencies (i.e., $f_{max}$ = +65.65 Hz and $f_{min}$ = -65.65 Hz).

Fig. 8 shows the PSDs and the exponential fitting corresponding to the measured data for LCM1 (see Fig. 8(a)) and LCM2 (see Fig. 8(b)). As can be observed in the figure, the measured data best fit in the center of the $x$-axis (i.e., for $f = 0$ Hz) in both cases. The main reason for this effect is that the measured data variability is higher when the Doppler frequency increases than in the principal component. In addition, the specific fitting parameters of these two examples are included in the PSD definitions of the following Eqs. (12) and (13):

$$S_{LCM1}(f) = \begin{cases} 13.9\,\exp(0.13f) - 42.1, & f_{min} \le f < 0 \\ \delta(f), & f = 0 \\ 13.3\,\exp(-0.12f) - 41.9, & 0 < f \le f_{max} \end{cases} \tag{12}$$

$$S_{LCM2}(f) = \begin{cases} 13.5\,\exp(0.08f) - 38.6, & f_{min} \le f < 0 \\ \delta(f), & f = 0 \\ 13.7\,\exp(-0.09f) - 38.2, & 0 < f \le f_{max} \end{cases} \tag{13}$$

LCM2 presents a lower exponential decay (see $b$ and $e$) than LCM1. Focusing on the mean value of $c$ and $g$ parameters, which gives an idea of the power density for the highest and lowest frequencies, it is slightly higher in LCM2.

In summary, the results presented in this section indicate that most of the Doppler spectrum density is concentrated in $f = 0$ Hz. In fact, in both Doppler PSDs (i.e., LCM1 and LCM2), increasing the Doppler frequency to $f = 1$ Hz implies a power fall of 20 dB, and they have an asymptotic behavior at around 40 dB. Therefore, we can assume that the observed loopback channel models are static. This conclusion may be generalized to other broadcast centers due to the similarities in the application use cases (i.e., fixed transmission and

**Table 3**
Empirical values of Delay Spread and K-factor.

| | $\tau_{mean}$ (ns) | $\tau_{RMS}$ (ns) | $K$-factor (dB) |
|---|---|---|---|
| LCM1 | 41.59 | 151.56 | 9.93 |
| LCM2 | 16.73 | 49.67 | 13.31 |

reception antennas, low reflective area, or high isolation). Nevertheless, the Doppler analysis may differ from Fig. 8 in non-broadcast use cases such as broadband communications (i.e., 5G/6G) since their application target is urban areas with many mobile users/objects. In addition, bad weather conditions such as wind and storms may also affect the Doppler spectrum due to the tower swinging. Nevertheless, conducting channel measurements in those weather conditions implies extremely high risk for the hardware equipment and technical workers who climb through the transmission tower. Consequently, channel modeling of bad weather conditions was not feasible in this work. However, for future work, these complex scenarios can be modeled as demonstrated in the study by Hong et al. [27]. Their work models the impact of tower swing due to wind on the Doppler spectrum. Consequently, the spectrum variations proposed by the authors could be integrated into the spectra defined in Eqs. (12) and (13).

### 4.3. Additional channel parameters: delay spread and K-factor

Most channel models provide Delay Spread and K-factor calculations. Those figures will describe the dispersion in time of the received energy at the receiver. In general, the Delay spread is used to analyze the relevance of the multipath propagation to the total received time energy.

The mean Delay Spread can be interpreted as an average metric to characterize the difference between the time of arrival of the earliest significant multipath component and the time of arrival of the last multipath components [67]. In addition to $\tau_{mean}$, the RMS delay spread is also used ($\tau_{RMS}$), which is also known as the root of the second central moment of the normalized delay power density spectrum. The reference equations for obtaining these parameters can be found in [68].

The calculation of the Delay Spread can be complemented with the fading K-factor. This parameter is defined as the ratio of signal power in the dominant component over the scattered and reflected signal power. Consequently, it determines the distribution of the received signal amplitude [69]. The K-factor calculation method considered here for reference comparison purposes is the one recommended by ETSI [61]. Table 3 summarizes Delay Spread's and K-factor's empirical results.

In general, LCM1 and LCM2 loopback channels present short delay spreads (mean delay spread below 50 ns in both cases). The maximum RMS delay spread is close to 150 ns. These results are compatible with the short distances between the transmitting and receiving antenna. In addition, it should also be highlighted that LCM2 presents an even shorter mean and RMS delay spread values if compared with LCM1. This result is in line with the measurements shown in Fig. 7 (solid blue line) since the channel impulse response of LCM1 shows a higher amplitude than LCM2 between 4 μs and 8 μs.

In both channels (LCM1 and LCM2), most of the received power is concentrated in the first path. Furthermore, it should also be noted that LCM2 has less power dispersion than LCM1 since the calculated K-factor is always more significant than that calculated for LCM1. These results align with the delay spread calculations, where LCM1 has shown a higher delay spread than LCM2 due to the channel impulse response amplitude between 4 μs and 8 μs.

## 5. Channel model performance evaluation

The main goal of this section is to measure the channel models' performance in realistic transceiver chains. Hence, we have implemented a complete ATSC 3.0 transmission-reception chain and tested all the proposed channel models to analyze how they affect the transmitted signal.

**Table 4**
Parameter summary of the ATSC 3.0 transceiver chain.

| Parameter | Value |
|---|---|
| Bandwidth | 6 MHz |
| FFT Size | 16 k |
| Guard Interval | 1/16 |
| Outer FEC | BCH |
| Inner FEC | LDPC |
| Modulation | QPSK, 16-NUC, 64-NUC |
| Code rate | 3/15, 7/15, 12/15 |
| Equalization | Ideal |
| MIMO | No |
| LDM | No |
| SNR step | 0.05 dB |
| #Seeds | 1000 |

Table 4 summarizes the most relevant parameters describing the simulated ATSC 3.0 transceiver. It should be highlighted that ATSC 3.0 uses two consecutive Forward Error Correction (FEC) techniques: Bose–Chaudhuri–Hocquenghem (BCH) as outer coding and Low-Density Parity-Check (LDPC) codes as inner coding. In addition, we have not considered optional configurations such as Multiple-Input Multiple-Output (MIMO) or Layered Division Multiplexing (LDM) to analyze the purest ATSC 3.0 structure and not to introduce additional effects to the transmission chain. Concerning the modulation and the code rate of the transmitted signal, three different configurations have been selected to test channel models combined with different signal robustness levels: QPSK 3/15 (high robustness and low data rate), 16-non uniform constellation (NUC) 10/15 (mid robustness and mid data rate), 64-NUC 12/15 (low robustness and high data rate).

Fig. 9 shows the results obtained with the four proposed channel models (see Table 2) in terms of bit error rate (BER) vs. signal-to-noise ratio (SNR). Each modulation and code rate configuration also includes the simulation of the AWGN channel model to use as a reference. The first evident takeaway from the results is that the proposed loopback channels affect the transmitted signal more strongly than the AWGN model. This means that for a fixed SNR value, all the LCM channels present a lower BER value. In particular, the difference between AWGN and the LCM models increases when the required SNR increases. While a variation below one dB is observed in Fig. 9(a), the difference increases up to three dB in Fig. 9(c). Another relevant conclusion is that using 6 or 12 taps to model the channel slightly affects the performance. The channel models based on six taps perform better than those based on 12. This effect is due to the location of the additional taps in the 12-tap models. In fact, when the number of taps used for channel modeling increases, the model shows a higher multipath effect. This issue was already detected in Table 2. Nevertheless, as the multipath effect can be considered short (between 5-7 μs in LCM1 and around 12 μs in LCM2), the influence of the number of taps in the channel modeling is always below one dB. The maximum difference can be observed when transmitting a 64-NUC 12/15 signal through LCM2. Finally, the last relevant conclusion obtained from Fig. 9 is the different performances regarding LCM1 and LCM2. The difference between LCM1 and LCM2 increases when the required SNR increases. Particularly, while very similar results are shown in Fig. 9(a), the variation between the models increases up to two dB in the low robustness configuration (see Fig. 9(c)). This conclusion aligns with the results observed during the delay spread calculation (see Table 3), where a higher multipath effect was detected in LCM1, and, therefore, the transmitted signal is more affected by the channel.

It is important to note that the performance curves shown in Fig. 9 assume ideal channel estimation. These curves illustrate performance and deviation relative to the AWGN channel, which is solely based on the channel structure. However, several channel-related parameters can influence these curves. For instance, if a different Doppler spectrum

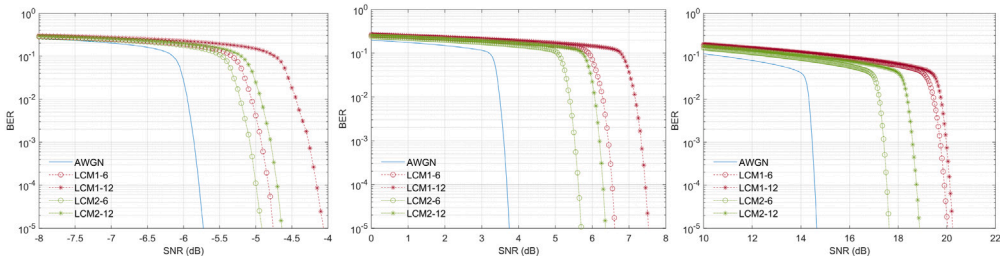


(a) QPSK 3/15 (b) 16-NUC 7/15 (c) 64-NUC 12/15

**Fig. 9.** Performance evaluation of the loopback channel models using an ATSC 3.0 transceiver. AWGN channel model is used as a reference.

model is used, it may result in slower convergence of the curves. This is particularly true when most Doppler power is not centered around $f = 0$ Hz. Another significant difference would arise from using a non-ideal channel estimation. In such cases, errors are introduced, which can be modeled as additional noise in the system. Consequently, this fact causes all cases to shift to the right in the graph, implying that a higher available SNR would be required for a given BER value. Nevertheless, a complete transmission-reception chain is required for a complete non-ideal self-interference cancellation. This implies a self-interference channel estimation and cancellation (non-ideal), followed by a channel estimation stage to recover the transmitted signal.

Finally, we have detailed some recommendations for the correct use of the measured channels based on the data shown in this section and on the field trial conditions:

- The four channels presented in this work describe loopback channels exclusively.
- Although both loopback channels present a similar delay-ampli tude path relation, the measurement configuration differed. Therefore, we recommend using LCM2 to replicate mountainous areas and LCM1 for the rest of the cases.
- For more realism, it is recommended to use the 12-tap-based channels. Consequently, the 6-tap channels are reserved for cases where channel complexity is a crucial requirement.

## 6. Conclusions

This article empirically characterizes the loopback channel for in-band full-duplex communications. In particular, the authors propose loopback channel models obtained in an operational broadcast transmission center. Two different channel models have been proposed depending on the orientation of the receiver antenna. Then, analysis and discussion are presented regarding several channel parameters, namely the Doppler spectrum, the delay spread, and the K-factor.

Different channel models are proposed here depending on the relevant paths (i.e., 6-taps and 12-taps). The characterization includes the definition of each path's amplitude and delay. During this process, we have concluded that most channel energy is concentrated in the first microsecond of the signal. Moreover, the last taps of LCM1 are located between 5-7 μs and around 12 μs in the case of LCM2. The delay spread analysis showed shallow values in both cases, although LCM1 had higher values than LCM2. The mean delay spread in both cases is below 50 ns, and the maximum RMS delay spread is below 150 ns. A similar conclusion is obtained from the K-factor analysis, where LCM1 presents a value 3–4 dB higher than LCM2. Finally, we have also analyzed the Doppler PSD of the loopback channel and concluded that the distribution that best fits the real Doppler spectrum is a Dirac delta for $f = 0$ Hz and exponential decay functions for the remaining frequency. This model means that most of the Doppler spectrum density is concentrated in $f = 0$ Hz; therefore, the loopback channel is almost static.

The analysis, definition, and characterization of the loopback channel model fill a gap that the in-band full-duplex communication designs have had during the last years. In fact, to the best of the authors' knowledge, this is the first paper presenting the characterization of a loopback channel model based on experimental measurements in an authentic and active broadcast facility. This study enlarges the knowledge of the full-duplex research community, especially in broadcast environments. In addition, the proposal of these new channel models provides a new tool for developing and validating in-band full-duplex solutions since any researcher can use them during the simulation stage or the channel emulation. Doubtlessly, using these channel models increases the realism of future full-duplex developments.

Since the study was conducted at a specific transmission center, and although it represents many current broadcast centers, future work is needed to ensure the models' suitability to other scenarios, such as MIMO environments. We have planned future work to broaden the study's applicability. We aim to repeat the measurements in other transmitter centers to compare and analyze the models' universality. Additionally, we will develop a characterization that incorporates the environment and can be replicated using ray tracing software.

## CRediT authorship contribution statement

**Iñigo Bilbao:** Conceptualization, Data curation, Investigation, Methodology, Writing – original draft, Writing – review & editing. **Eneko Iradier:** Writing – review & editing, Writing – original draft, Methodology, Investigation, Data curation. **Marta Fernandez:** Methodology. **Jon Montalban:** Investigation, Conceptualization. **Pablo Angueira:** Supervision, Conceptualization. **Zhihong Hunter Hong:** Formal analysis. **Yiyan Wu:** Supervision, Conceptualization.

## Declaration of competing interest

The authors declare that they have no known competing financial interests or personal relationships that could have appeared to influence the work reported in this paper.

## Data availability

The data that has been used is confidential.

## Acknowledgments

This work was supported by the Basque Government, Spain (under the grant IT1436-22 and the grant Elkartek KK-2022/00069) and by the Spanish Government under the grant PID2021-124706OB-I00 funded by MCIN/AEI/ 10.13039/501100011033 and by ERDF A way of making Europe. We want to thank the company Itelazpi for the help, time, equipment, and access to the broadcast infrastructure provided. Without their help, this work would not have been possible.

## References


[1] D. Song, J. Ren, L. Wang, G. Chen, Designing a common dp-ldpc code pair for variable on-body channels, IEEE Trans. Wireless Commun. (2022) 1.

[2] D. Song, L. Wang, Z. Xu, G. Chen, Joint code rate compatible design of dp-ldpc code pairs for joint source channel coding over implant-to-external channel, IEEE Trans. Wireless Commun. 21 (7) (2022) 5526–5540.

[3] Y. Yapici, I. Guven, H. Dai, Low-resolution limited-feedback noma for mmwave communications, IEEE Trans. Wireless Commun. 19 (8) (2020) 5433–5446.

[4] F. Wu, L. Chen, N. Zhao, Y. Chen, F. Richard Yu, G. Wei, Noma-enhanced computation over multi-access channels, IEEE Trans. Wireless Commun. 19 (4) (2020) 2252–2267.

[5] K. Xiao, B. Xia, Z. Chen, B. Xiao, D. Chen, S. Ma, On capacity-based codebook design and advanced decoding for sparse code multiple access systems, IEEE Trans. Wireless Commun. 17 (6) (2018) 3834–3849.

[6] D. Capriglione, G. Cerro, L. Ferrigno, G. Miele, Performance analysis of a two-stage spectrum sensing scheme for dynamic spectrum access in TV bands, Measurement 135 (2019) 661–671.

[7] D. Kim, H. Lee, D. Hong, A survey of in-band full-duplex transmission: From the perspective of phy and mac layers, IEEE Commun. Surv. Tutor. 17 (4) (2015) 2017–2046.

[8] A. Kurt, M.B. Salman, U.B. Sarac, G.M. Guvensen, An adaptive-iterative nonlinear interference cancellation in time-varying full-duplex channels, IEEE Trans. Veh. Technol. (2022).

[9] S. Liu, L. Lin, M. Ma, B. Jiao, Improved fractional delay method for canceling the self-interference of full duplex, IEEE Trans. Veh. Technol. (2022).

[10] A. Sabharwal, P. Schniter, D. Guo, D.W. Bliss, S. Rangarajan, R. Wichman, In-band full-duplex wireless: Challenges and opportunities, IEEE J. Sel. Areas Commun. 32 (9) (2014) 1637–1652.

[11] J. Hu, B. Di, Y. Liao, K. Bian, L. Song, Hybrid mac protocol design and optimization for full duplex wi-fi networks, IEEE Trans. Wireless Commun. 17 (6) (2018) 3615–3630.

[12] L.Y. Erol, A. Uzun, M. Seyyedesfahlan, I. Tekin, Broadband full-duplex antenna for ieee 802.11 protocols, IEEE Antennas Wirel. Propag. Lett. 20 (10) (2021) 1978–1982.

[13] M.S. Amjad, F. Dressler, Performance insights on ieee 802.11 a/g compliant software-based in-band full duplex relay systems, in: 2019 IEEE Wireless Communications and Networking Conference, WCNC, IEEE, 2019, pp. 1–7.

[14] L.H. Vu, R. Mareta, J.-H. Yun, Full-duplex wireless lan incorporating successive interference cancellation, IEEE Trans. Veh. Technol. 70 (10) (2021) 10293–10307.

[15] T.N. Nguyen, et al., Outage performance of satellite terrestrial full-duplex relaying networks with co-channel interference, IEEE Wirel. Commun. Lett. 11 (7) (2022) 1478–1482.

[16] M.R. Bhavani Shankar, Gan Zheng, S. Maleki, B. Ottersten, Feasibility study of full-duplex relaying in satellite networks, in: 2015 IEEE 16th International Workshop on Signal Processing Advances in Wireless Communications, SPAWC, Stockholm, Sweden, 2015, pp. 560–564.

[17] Z. Al-Makhadmeh, A. Tolba, Coalition-based interference mitigation method for wearable sensor transmitter–receiver antenna communications, Measurement 182 (2021) 1–12.

[18] Z.A. Jaaz, I.Y. Khudhair, H.S. Mehdy, I. Al Barazanchi, Imparting full-duplex wireless cellular communication in 5 g network using apache spark engine, in: 2021 8th International Conference on Electrical Engineering, Computer Science and Informatics, EECSI, IEEE, 2021, pp. 123–129.

[19] H. Alves, R.D. Souza, M.E. Pellenz, Brief survey on full-duplex relaying and its applications on 5 g, in: 2015 IEEE 20th International Workshop on Computer Aided Modelling and Design of Communication Links and Networks, CAMAD, IEEE, 2015, pp. 17–21.

[20] M. Fakih, A. Diallo, P. Le Thuc, R. Staraj, O. Mourad, E. Rachid, Characteristic mode theory to enhance the isolation level for fullduplex 5 g in mobile handsets, in: 2019 16th International Symposium on Wireless Communication Systems, ISWCS, IEEE, 2019, pp. 81–85.

[21] X. Zhang, W. Cheng, H. Zhang, Full-duplex transmission in phy and mac layers for 5 g mobile wireless networks, IEEE Wirel. Commun. 22 (5) (2015) 112–121.

[22] R. Cabrera, O. Landrove, E. Iradier, P. Angueira, J. Montalban, Broadcast Core Network (BCN): Paving the future path of DTT, IEEE Commun. Mag. 61 (7) (2023) 120–126.

[23] L. Zhang, W. Li, Y. Wu, S. Lafleche, Z. Hong, S.-I. Park, J.-Y. Lee, H.-M. Kim, N. Hur, E. Iradier, et al., Using layered division multiplexing for wireless in-band distribution links in next generation broadcast systems, IEEE Trans. Broadcast. 67 (1) (2020) 68–82.

[24] L. Zhang, Y. Wu, W. Li, S.-I. Park, J.-y. Lee, H.-M. Kim, N. Hur, E. Iradier, P. Angueira, J. Montalban, Atsc 3.0 in-band backhaul for sfn using ldm with full backward compatibility, in: 2019 IEEE International Symposium on Broadband Multimedia Systems and Broadcasting, BMSB, 2019, pp. 1–6.

[25] W. Li, L. Zhang, Y. Wu, Z. Hong, S. Lafl'eche, S.-I. Park, S. Kown, S. Ahn, N. Hur, E. Iradier, I. Bilbao, J. Montalban, P. Angueira, Integrated inter-tower wireless communications network for terrestrial broadcasting and multicasting.

[26] J. Montalban, R. Cabrera, E. Iradier, P. Angueira, Y. Wu, L. Zhang, W. Li, Z. Hong, Broadcast core-network: Converging broadcasting with the connected world, IEEE Trans. Broadcast. 67 (3) (2021) 558–569.

[27] Z. Hong, L. Zhang, W. Li, Y. Wu, S.-I. Park, S. Ahn, S. Kwon, N. Hur, E. Iradier, J. Montalban, P. Anguiera, In-band distribution link signal detection in atsc 3.0, in: 2021 IEEE International Symposium on Broadband Multimedia Systems and Broadcasting, BMSB, 2021, pp. 1–6.

[28] W. Slingsby, J. McGeehan, Antenna isolation measurements for on-frequency radio repeaters, in: 1995 Ninth International Conference on Antennas and Propagation, Vol. 1, ICAP'95 (Conf. Publ. No. 407), IET, 1995, pp. 239–243.

[29] C.R. Anderson, S. Krishnamoorthy, C.G. Ranson, T.J. Lemon, W.G. Newhall, T. Kummetz, J.H. Reed, Antenna isolation, wideband multipath propagation measurements, and interference mitigation for onfrequency repeaters, in: IEEE SoutheastCon, 2004. Proceedings, IEEE, 2004, pp. 110–114.

[30] Z.H. Hong, L. Zhang, W. Li, Y. Wu, Z. Zhu, S.-I. Park, S. Ahn, S. Kwon, N. Hur, E. Iradier, et al., Frequency-domain rf self-interference cancellation for in-band full-duplex communications, IEEE Trans. Wireless Commun. (2022).

[31] H. Yang, H. Zhang, J. Zhang, L. Yang, Digital self-interference cancellation based on blind source separation and spectral efficiency analysis for the full-duplex communication systems, IEEE Access 6 (2018) 43946–43955.

[32] X. Quan, Y. Liu, D. Chen, S. Shao, Y. Tang, K. Kang, Blind nonlinear self-interference cancellation for wireless full-duplex transceivers, IEEE Access 6 (2018) 37725–37737.

[33] K.E. Kolodziej, J.G. McMichael, B.T. Perry, Multitap rf canceller for in-band full-duplex wireless communications, IEEE Trans. Wireless Commun. 15 (6) (2016) 4321–4334.

[34] Y. Liu, X. Quan, S. Shao, Y. Tang, Digital predistortion architecture with reduced adc dynamic range, Electron. Lett. 52 (6) (2016) 435–437.

[35] K.E. Kolodziej, B.T. Perry, J.S. Herd, In-band full-duplex technology: Techniques and systems survey, IEEE Trans. Microw. Theory Tech. 67 (7) (2019) 3025–3041.

[36] M. Portela, M. Vera-Isasa, M. Garcia Sanchez, Self-interference suppression improvement by employing circular polarized antennas, Measurement 110 (2017) 53–59.

[37] M. Duarte, A. Sabharwal, Full-duplex wireless communications using off-the-shelf radios: Feasibility and first results, in: 2010 Conference Record of the Forty Fourth Asilomar Conference on Signals, Systems and Computers, Pacific Grove, CA, USA, 2010, pp. 1558–1562.

[38] M. Duarte, et al., Design and characterization of a full-duplex multiantenna system for WiFi networks, IEEE Trans. Veh. Technol. 63 (3) (2014) 1160–1177.

[39] D. Korpi, M. Heino, C. Icheln, K. Haneda, M. Valkama, Compact inband full-duplex relays with beyond 100 db self-interference suppression: Enabling techniques and field measurements, IEEE Trans. Antennas and Propagation 65 (2) (2017) 960–965.

[40] E. Iradier, I. Bilbao, M. Fernandez, J. Montalban, Z. Hong, L. Zhang, W. Li, Y. Wu, Signal isolation in full-duplex inter-tower communication networks: Field trials, in: 2022 IEEE International Symposium on Broadband Multimedia Systems and Broadcasting, BMSB, 2022, pp. 1–6.

[41] E. Iradier, I. Bilbao, J. Montalban, Y. Wu, L. Zhang, W. Li, Z. Hong, Analog cancellation in atsc 3.0 for enabling inter-tower communications network, in: 2021 IEEE International Symposium on Broadband Multimedia Systems and Broadcasting, BMSB, IEEE, 2021, pp. 1–6.

[42] R.V.C. Raro, G.G. Mendoza, M.F. De Guzman, Analog domain cancellation in hybrid self-interference cancellers for in-band full-duplex radios, in: 2019 IEEE Asia-Pacific Microwave Conference, APMC, IEEE, 2019, pp. 646–648.

[43] S.B. Venkatakrishnan, E.A. Alwan, J.L. Volakis, Wideband rf self-interference cancellation circuit for phased array simultaneous transmit and receive systems, IEEE Access 6 (2018) 3425–3432.

[44] A.T. Le, X. Huang, Y.J. Guo, et al., Analog least mean square loop with i/q imbalance for self-interference cancellation in full-duplex radios, IEEE Trans. Veh. Technol. 68 (10) (2019) 9848–9860.

[45] T. Matsumura, On the analog self-interference cancellation for in-band full-duplex radio with compensation for inherent frequency response, in: 2021 24th International Symposium on Wireless Personal Multimedia Communications, WPMC, IEEE, 2021, pp. 1–6.

[46] B. Debaillie, D.-J. van den Broek, C. Lavin, B. van Liempd, E.A. Klumperink, C. Palacios, J. Craninckx, B. Nauta, A. Pärssinen, Analog/rf solutions enabling compact full-duplex radios, IEEE J. Sel. Areas Commun. 32 (9) (2014) 1662–1673.

[47] R. Sepanek, M. Hickle, M. Stuenkel, In-band full-duplex selfinterference canceller augmented with bandstop-configured resonators, in: 2020 IEEE/MTT-S International Microwave Symposium, IMS, IEEE, 2020, pp. 1199–1202.

[48] F.A. Tripta, S.B.A. Kumar, T.C.S. Saha, Wavelet decomposition based channel estimation and digital domain self-interference cancellation in in-band full-duplex ofdm systems, in: 2019 URSI Asia-Pacific Radio Science Conference, AP-RASC, IEEE, 2019, pp. 1–4.

[49] H. Wu, Y. Wang, Z. Li, X. Jin, A novel variable tap-length digital self-interference cancellation algorithm for full-duplex system, in: 2019 IEEE 2nd International Conference on Automation, Electronics and Electrical Engineering, AUTEEE, IEEE, 2019, pp. 424–427.

[50] H. Li, J. Van Kerrebrouck, O. Caytan, H. Rogier, J. Bauwelinck, P. Demeester, G. Torfs, Self-interference cancellation enabling high-throughput short-reach wireless full-duplex communication, IEEE Trans. Wireless Commun. 17 (10) (2018) 6475–6486.
[51] E. Ahmed, A.M. Eltawil, All-digital self-interference cancellation technique for full-duplex systems, IEEE Trans. Wireless Commun. 14 (7) (2015) 3519–3532.
[52] H. Ayar, O. Gurbuz, Cyclic prefix noise reduction for digital self interference cancellation in ofdm-based in-band full-duplex wireless systems, IEEE Trans. Wireless Commun. 20 (9) (2021) 6224–6238.
[53] I. Angulo, J. Montalban, J. Canizo, Y. Wu, D. de la Vega, D. Guerra, P. Angueira, A. Arrinda, Empirical doppler characterization of signals scattered by wind turbines in the uhf band under near field condition, Int. J. Antennas Propag. 2013 (2013).
[54] I. Angulo, J. Montalban, J. Canizo, Y. Wu, D. de la Vega, D. Guerra, P. Angueira, A. Arrinda, A measurement-based multipath channel model for signal propagation in presence of wind farms in the uhf band, IEEE Trans. Commun. 61 (11) (2013) 4788–4798.
[55] C.-L. Cheng, S. Sangodoyin, A. Zajic, Thz cluster-based modeling and propagation characterization in a data center environment, IEEE Access 8 (2020) 56544–56558.
[56] D. Yan, K. Guan, D. He, B. Ai, Z. Li, J. Kim, H. Chung, Z. Zhong, Channel characterization for vehicle-to-infrastructure communications in millimeter-wave band, IEEE Access 8 (2020) 42325–42341.
[57] P. Bello, Characterization of randomly time-variant linear channels, IEEE Trans. Commun. Syst. 11 (4) (1963) 360–393.
[58] Itelazpi – digitalizaziorako funtsezkoak — Esenciales para la digitalizaci'on, 2024, Itelazpi. https://www.itelazpi.eus/es/ (Accessed 20 February 2024).
[59] Promax, PROMAX DIGITAL TO TV DT-730, 2014, 0 MI2039 datasheet, Dec. 2014 [Revised Feb. 2024].
[60] G. Prieto, D. Ansorregui, C. Regueiro, J. Montalban, I. Eizmendi, M. Velez, Platform for advanced dvb-t2 system performance measurement, in: 2013 IEEE International Symposium on Broadband Multimedia Systems and Broadcasting, BMSB, IEEE, 2013, pp. 1–7.
[61] ETSI 102 831 V1. 2.1, Implementation Guidelines for a Second Generation Digital Terrestrial Television Broadcasting System (DVB-T2), Geneva, 2012.
[62] R. Candell, C.A. Remley, J.T. Quimby, D.R. Novotny, A. Curtin, P.B. Papazian, G.H. Koepke, J. Diener, M.T. Hany, et al., Industrial wireless systems: Radio propagation measurements, 2017.
[63] ETSI TR 102 377, Digital Video Broadcasting (DVB); DVB-H Implementation Guidelines, Geneva, 2005.
[64] F. Vatalaro, A. Forcella, Doppler spectrum in mobile-to-mobile communications in the presence of three-dimensional multipath scattering, IEEE Trans. Veh. Technol. 46 (1) (1997) 213–219.
[65] G. Acosta, K. Tokuda, M.A. Ingram, Measured joint doppler-delay power profiles for vehicle-to-vehicle communications at 2.4 ghz, in: IEEE Global Telecommunications Conference, 2004, Vol. 6, GLOBECOM'04, IEEE, 2004, pp. 3813–3817.
[66] X. Zhao, J. Kivinen, P. Vainikainen, K. Skog, Characterization of doppler spectra for mobile communications at 5.3 ghz, IEEE Trans. Veh. Technol. 52 (1) (2003) 14–23.
[67] E.S. Sousa, V.M. Jovanovic, C. Daigneault, Delay spread measurements for the digital cellular channel in toronto, IEEE Trans. Veh. Technol. 43 (4) (1994) 837–847.
[68] K. Hassan, T. Rahman, M. Kamarudin, F. Nor, The mathematical relationship between maximum access delay and the rms delay spread, in: The Seventh International Conference on Wireless and Mobile Communications, ICWMC 2011, Luxembourg, 2011, pp. 18–23.
[69] C. Tepedelenlioglu, A. Abdi, G.B. Giannakis, The ricean k factor: estimation and performance analysis, IEEE Trans. Wireless Commun. 2 (4) (2003) 799–810.